

Spin orbit torque-driven motion of quasi-Bloch domain wall in perpendicularly magnetized W/CoFeB/MgO structures

Nobuyuki Umetsu, Michael Quinsat, Susumu
Hashimoto, Tsuyoshi Kondo, and Masaki Kado

*Frontier Technology R&D institute,
Kioxia Corporation, Yokohama, Japan.*

(Dated: November 4, 2024)

arXiv:2411.00516v1 [cond-mat.mes-hall] 1 Nov 2024

Abstract

The motion of chiral magnetic domain walls (DWs) driven by spin-orbit torque (SOT) has been extensively studied in heavy metal/ferromagnet heterostructures with perpendicular magnetic anisotropy. This study specifically focuses on SOT-driven DWs in near Bloch-states, which we refer to as “quasi-Bloch DWs”. These quasi-Bloch DWs exhibit slower motion compared to Neel-type DWs, offering potential for achieving highly controllable DW positions. Here, we investigate the characteristics of SOT-driven motion of quasi-Bloch DWs in perpendicularly magnetized ultra-thin films consisting of W/CoFeB/MgO. For analyzing the DW motion, we employ a one-dimensional model incorporating parameters derived from experimental data obtained from our samples. Our model successfully reproduces the experimental results, which reveal variations in the direction and threshold current density of DW motion among different samples. Through theoretical analysis, we unveil that the DW remains in quasi-Bloch states during motion, with SOT serving as the primary driving force rather than spin transfer torque (STT). The direction of motion is determined not only by the sign combination of Dzyaloshinskii-Moriya interaction (DMI) and spin Hall angle but also by the strength of DMI, STT, and extrinsic DW pinning. Furthermore, we provide analytical expressions for the threshold current density required for SOT-driven quasi-Bloch DW motion. These findings provide valuable insights for the design of future DW devices with specific film structures.

I. INTRODUCTION

The phenomenon of chiral magnetic domain wall (DW) motion driven by spin-orbit torque (SOT) has been extensively studied in heavy metal (HM)/ferromagnet (FM) heterostructures with perpendicular magnetic anisotropy [1–11]. SOT offers the potential to drive DWs faster than conventional spin transfer torque (STT) [12–17] and at lower currents [18, 19].

The characteristics of SOT-driven DW motion are influenced by both the properties of SOT and the DW structure [20, 21], which is governed by the Dzyaloshinskii-Moriya interaction (DMI) at the HM/FM interface. In theory, SOT affects the DW motion except when it is in a perfect Bloch-state. The strength of SOT acting on the DW is greater when the DW is closer to a Neel-state, resulting in higher DW velocities. The direction of SOT-driven DW motion is determined by the combination of the DW chirality and the sign of

the spin Hall angle (SHA) [22]. When the DW is close to Neel-states, the chiral direction is determined by the sign of DMI, but when the DW is close to Bloch-states, the chiral direction can also be influenced by STT and extrinsic DW pinning. However, previous studies have not provided a comprehensive interpretation of the experimental results regarding the direction of DW motion from this standpoint. Although the fast SOT-driven motion of Neel-type DWs is intriguing, it may not be suitable for precise control of DW positions in integrated circuit devices. Conversely, SOT-driven motion of DWs in near Bloch-states, which we refer to as “quasi-Bloch DWs”, offers slower motion that is better suited for practical applications.

In this study, we investigate the characteristics of SOT-driven motion of quasi-Bloch DWs in perpendicularly magnetized ultra-thin films consisting of W/CoFeB/MgO. We experimentally examine the magnetic film properties, efficiencies of SOT, and current-induced DW motion (CIDWM). By utilizing these experimental values, we perform model calculations that incorporate not only SOT and DMI but also STT and the depinning magnetic field [23, 24] as a substitute for extrinsic DW pinning. Our model successfully reproduces the experimental results, which reveal variations in the direction and threshold current density of DW motion among different samples. Our theoretical analysis reveals that the DW remains in near Bloch-states during SOT-driven motion. Additionally, we identify the key factors influencing the direction of DW motion and provide analytical expressions for the threshold current density of DW motion. These findings are of utmost importance for the design of future DW devices’ film structures [25].

The remainder of this paper is organized as follows: In Sec. II, we present the characterization of our samples based on the measurement results of magnetic film properties, SOT efficiencies, and CIDWM. In Sec. III, we present our model and demonstrate its capability to reproduce the experimental results, which reveal variations in the direction and threshold current density of DW motion among different samples. In Sec. IV, we discuss the direction, speed, and threshold current density of SOT-driven motion for quasi-Bloch DWs based on our model. We specifically focus on the influence of STT, DMI, and extrinsic DW pinning on the motion characteristics. Finally, we summarize our findings in Sec. V.

II. SAMPLE CHARACTERIZATION

In this study, we used ultra-thin films consisting of $\text{Al}_2\text{O}_3(20 \text{ nm})/\text{W}(2 \text{ nm})/\text{Co}_{40}\text{Fe}_{40}\text{B}_{20}(1-1.3 \text{ nm})/\text{MgO}(2 \text{ nm})/\text{TaN}(1 \text{ nm})$. The films were deposited onto thermally oxidized Si substrates using a magnetron sputter deposition system with a base pressure of less than $5 \times 10^{-6} \text{ Pa}$. The deposition pressures for W and CoFeB layers were 0.04-0.5 Pa and 0.27 Pa, respectively. The samples were annealed at 300 °C or 400 °C in a vacuum for 1 hour. The thickness of the CoFeB layer (t_{CFB}), the deposition pressure of the W layer (P_{W}), and the annealing temperature (T_{a}) for each sample are summarized in Table I.

Sample	t_{CFB} (nm)	P_{W} (Pa)	T_{a} (°C)
A	1.2	0.27	300
B	1.3	0.5	300
C	1.0	0.04	400
D	1.1	0.04	400
E	1.2	0.27	400

TABLE I. Deposition conditions for each sample.

We evaluated various magnetic film properties and SOT efficiencies. The saturation magnetization, M_{s} and the effective perpendicular magnetic anisotropy, K_{eff} were measured using vibrating sample magnetometry (VSM). The magnetization curves measured by VSM are shown in Appendix A.

The STT efficiency is estimated using the obtained values of M_{s} and K_{eff} with the following equation:

$$\xi_{\text{ST}} = -\frac{\hbar P}{2\mu_0\gamma|e|M_{\text{s}}\lambda}, \quad (1)$$

where, μ_0 is the magnetic permeability, γ is the gyromagnetic ratio, e is the elementary charge, \hbar is the Dirac constant, P is the spin polarization, and $\lambda = \sqrt{A/K_{\text{eff}}}$ is the half width of the DW (with A as the exchange stiffness constant). For the estimation, we assume typical values of $A = 15 \text{ pJ/m}$ [24, 26] and $P = 0.5$.

We determined the depinning magnetic field, H_{dep} , through magnetic bubble domain expansion experiments [23, 24, 27]. The detailed method and measurement data are provided

in Appendix B. The value of H_{dep} is defined as the boundary value between the pinning-dependent thermally activated creep regime and the depinning transition regime. Since H_{dep} corresponds to the threshold field for DW depinning at zero temperature [27], we consider this value as a substitute for the extrinsic DW pinning field in our model, as discussed in the next section.

The DMI field, H_{DMI} were also obtained through magnetic bubble domain expansion experiments [28–30]. The measurement data are provided in Appendix C. The DMI constant is evaluated using

$$D = \mu_0 M_s \lambda H_{\text{DMI}}. \quad (2)$$

We determined the Slonczewski and field-like components of SOT efficiencies, ξ_{SL} and ξ_{FL} , using harmonic Hall voltage measurements [31–33]. The detailed method and measurement data for the harmonic Hall voltage measurements are provided in Appendix D. When estimating $\xi_{\text{SL(FL)}}$, it is necessary to account for the planar Hall effect (PHE) in addition to the anomalous Hall effect (AHE) if the Hall voltage includes contributions from both [31]. We assume a PHE resistance to AHE resistance ratio of 0.3 [34]. In the subsequent section, we demonstrate that the PHE contribution to the discussion in this study is negligibly small.

The spin Hall angle (Θ_{SH}) and the ratio of the field-like torque to the Slonczewski torque (β) are evaluated using the experimental values of $\xi_{\text{SL(FL)}}$ with the following equations:

$$\xi_{\text{SL}} = \frac{\hbar \Theta_{\text{SH}}}{2\mu_0 \gamma |e| M_s t_{\text{CFB}}}, \quad \xi_{\text{FL}} = \beta \xi_{\text{SL}}. \quad (3)$$

Here, we assume that the same current density occurs in both the CoFeB and W layers.

Figure 1(a)-(j) show the magnetic film properties and parameters related to current-induced spin torques for each sample. The values of K_{eff} , ξ_{ST} , H_{dep} , H_{DMI} , and D can be classified into two categories according to T_a . The higher value of K_{eff} for $T_a = 400^\circ\text{C}$ compared to $T_a = 300^\circ\text{C}$ can be attributed to the improvement in the crystallinity of CoFeB and MgO [35]. The increase in K_{eff} leads to an increase in $|\xi_{\text{ST}}|$ due to a decrease in the estimated value of λ . Additionally, the increase in K_{eff} may result in an increased spatial dispersion of K_{eff} , which causes an increase in H_{dep} due to enhanced extrinsic pinning for DW motion [36–38]. The correlation between DMI and K_{eff} has been reported not only in W/CoFeB/MgO structures [39] but also in other structures [40–42]. This implies that the interfacial spin-orbit coupling (SOC) is responsible for both DMI and K_{eff} . Kim *et al.*

suggest that the correlation originates from the SOC at the W/CoFeB interface, and these quantities have the same transformation mechanism during thermal treatment [39].

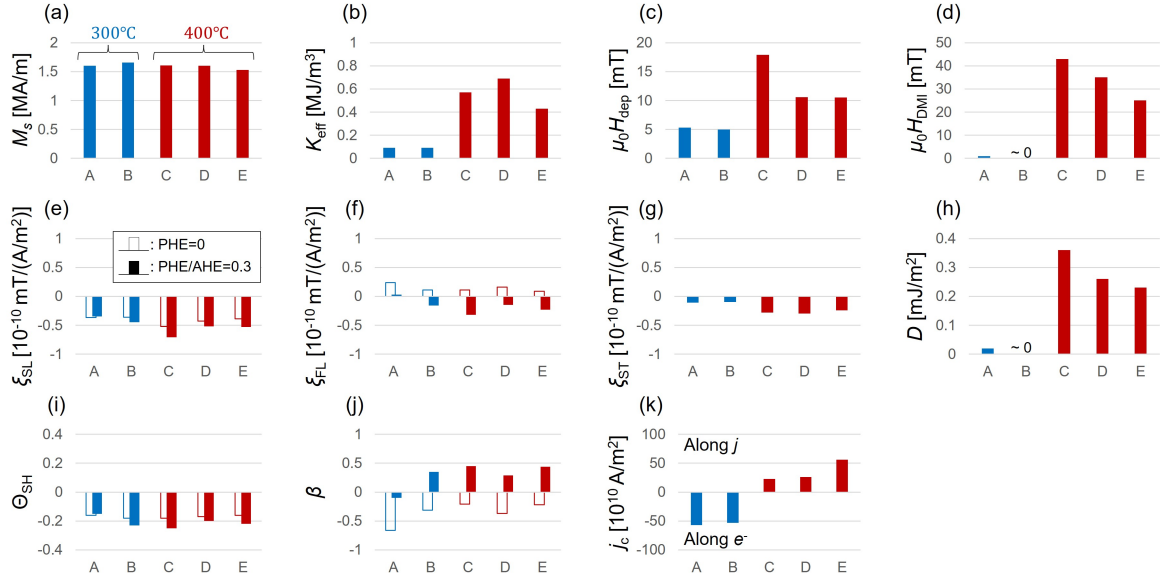


FIG. 1. (a)-(j) Magnetic film properties and parameters related to current-induced spin torques for each sample. The magnetic dead layer of 0.3 nm is taken into account in these estimations (See A). (k) Threshold current density for DW motion.

We observed CIDWM [43] and determined the threshold current density for DW motion for each sample. These experiments were carried out using a 2 μm wide ultra-thin wire, as shown in Fig. 2(a). Changes in the DW position were observed using a magneto-optical microscope when multiple pulses of 20 ns width were applied, as shown in Fig. 2(b).

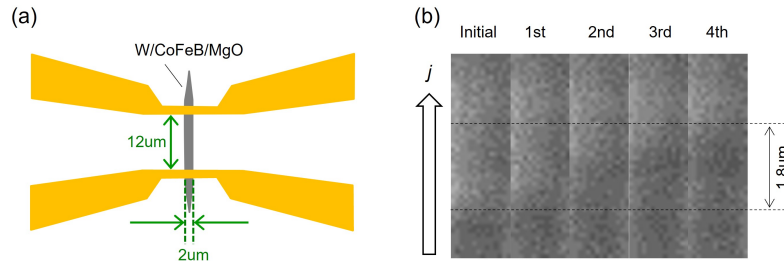


FIG. 2. (a) Schematic illustration of magnetic nanowire in CIDWM experiments. (b) Example of measured magnetic domain image.

Figure 1(k) shows the threshold current density, j_c for DW motion. The sign of j_c denotes the direction of DW motion. We observe that DW moves in the direction of electron flow

in samples annealed at 300 °C and in the direction of current flow in samples annealed at 400 °C. In Ta/CoFeB/MgO and Pt/CoFeB/MgO structures, both directions of DW motion have also been observed [5, 35, 44]. In situations where the DW is locked in near Neel-states by strong DMI ($D \gg 0.1 \text{ mJ/m}^2$), the direction of DW motion is consistent with the sign combination of D and SHA [22]. However, our experimental results cannot be explained using the same logic because D is nearly 0 in samples annealed at 300 °C. In Sec. IV, we theoretically elucidate the mechanism of DW motion parallel to the electron flow in such situations where the DW is in near Bloch-states.

III. MODEL

Assuming the uniformity of the DW cross section perpendicular to the direction of its motion, the dynamics of the DW can be described by the one-dimensional model (1DM) [38, 45, 46]. In this model, the DW motion is represented by the position (X) and the magnetization angle (ϕ), where $\phi = 0$ and π correspond to Neel-type DWs, and $\phi = \pm\pi/2$ correspond to Bloch-type DWs. These time-dependent variables are governed by the following equations:

$$\frac{d\phi}{dt} = \frac{\gamma}{1 + \alpha^2} [-Q\Gamma_1(\phi, X) - \alpha\Gamma_2(\phi, X)], \quad (4a)$$

$$\frac{d(X/\lambda)}{dt} = \frac{\gamma}{1 + \alpha^2} [-\alpha\Gamma_1(\phi, X) + Q\Gamma_2(\phi, X)], \quad (4b)$$

$$\Gamma_1(\phi, X) = Q\frac{\pi}{2}\xi_{\text{SL}}j \cos \phi + H_p(X), \quad (4c)$$

$$\Gamma_2(\phi, X) = Q\xi_{\text{ST}}j + \frac{\pi}{2}QH_{\text{DMI}} \sin \phi - \frac{\pi}{2}\xi_{\text{FL}}j \cos \phi - \frac{1}{2}H_a \sin 2\phi, \quad (4d)$$

where, α is the Gilbert damping constant, Q is the topological charge of the wall ($Q = +1$ for $\uparrow\downarrow$ wall and $Q = -1$ for $\downarrow\uparrow$ wall), j is the current density ($j > 0$ is considered in this article), $H_a = \ln 2M_s t_{\text{CFB}} / (\pi\lambda)$ is the shape anisotropy field, and $H_p(X)$ is the extrinsic DW pinning field which depends on the DW position. We use the value of $\alpha = 0.03$, which was experimentally determined by broadband ferromagnetic resonance measurements [47] for sample-E. Assuming that the annealing temperature dependence of α is not significant [48], we apply this value to all samples in our analysis.

Although STT and extrinsic DW pinning are often neglected when focusing on the qualitative behavior of SOT-driven DW motion [20, 21], this study considers these terms for

quantitative discussion. We assume a sinusoidal pinning potential [7, 35, 49] and express the extrinsic DW pinning field as $H_p(X) = H_{\text{pin}} \sin \frac{2\pi X}{L_{\text{pin}}}$, where H_{pin} is the amplitude and L_{pin} is the periodic length. Although direct measurement methods for H_{pin} and L_{pin} have not been established, H_{dep} is used as a substitute for H_{pin} . Additionally, based on the correlation length reported in the previous study [23], we assume $L_{\text{pin}} = 20 \text{ nm}$ [50].

Figure 3 compares the experimental results of j_c with the calculation results obtained from the 1DM simulation. Results of the DW velocity as a function of current density are shown in Appendix E. The direction of DW motion agrees between the experiments and simulations, both with and without PHE correction. The reason why $|j_c|$ with PHE correction is smaller than that without PHE correction is mainly because $|\Theta_{\text{SH}}|$ is larger with PHE correction. There is a positive correlation between the experimental and simulated values, and the magnitudes are of the same order. These results support the validity of our model, which includes not only SOT and DMI but also STT and H_{dep} .

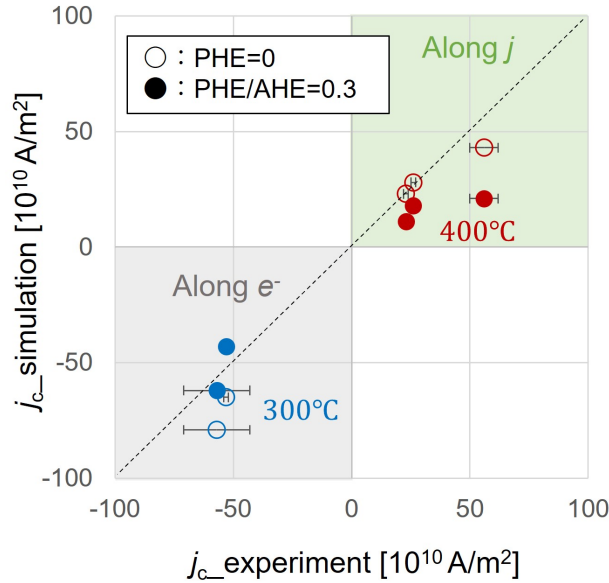


FIG. 3. Comparison of experimental results with j_c obtained by 1DM simulation.

IV. MOTION OF QUASI-BLOCH DOMAIN WALL

To clarify the behavior of quasi-Bloch DW motion in the presence of SOT, we present the calculation results of CIDWM in the range of $D = 0-0.2 \text{ mJ/m}^2$ and $\mu_0 H_{\text{pin}} = 0-20 \text{ mT}$.

For the other parameters, we use the fixed values shown in Table II, which are closed to the obtained values for the samples in this study.

t_{CFB}	M_s	λ	Θ_{SH}	β_{SH}	P	α	Q
1 nm	1.5 MA/m	7 nm	-0.2	0.4	0.5	0.03	+1

TABLE II. Fixed parameters in model analysis.

As an example of the DW dynamics, Fig. 4 shows the calculation results for $j = 50 \times 10^{10}$ A/m². The DW moves in the direction of current flow for $D \geq 0.1$ mJ/m², but in the direction of electron flow for $D = 0$. Except for $D = 0.2$ mJ/m², the DW can stop halfway in the case of strong extrinsic DW pinning ($\mu_0 H_{\text{pin}} = 10$ mT). During the DW motion in the presence of extrinsic DW pinning, the oscillatory behaviors of X and ϕ reflect the periodicity of $H_p(X)$. The larger the DW velocity, the shorter the oscillation period.

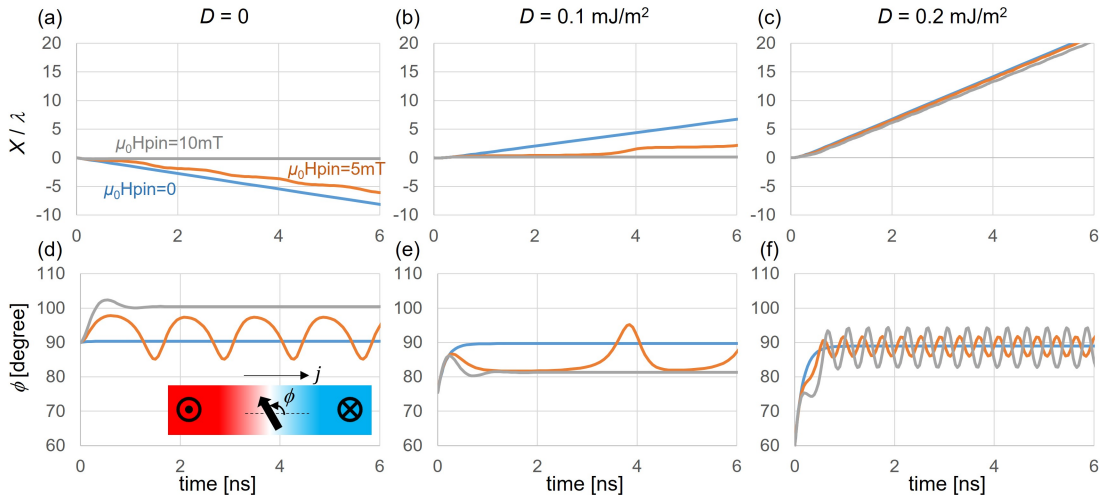


FIG. 4. (a)-(c) Transient of DW position normalized by the width of DW. (d)-(f) Transient of DW magnetization angle. $j = 50 \times 10^{10}$ A/m² is applied.

Figure 5 shows the DW velocity as a function of the current density (v - j curve). In the case of $D = 0$, the DW only moves in the direction of electron flow, and the DW speed increases with increasing j . However, in certain cases with $D > 0$, the DW can move in the direction of current flow. For example, in the case of $D = 0.2$ mJ/m², the DW speed initially increases with j in regions where j is small, but after a certain point, the DW speed decreases with j . This behavior is consistent with the previous calculation results [26, 46].

In the case of $D = 0.1 \text{ mJ/m}^2$, the v - j curve for $\mu_0 H_{\text{pin}} = 10 \text{ mT}$ is similar to that for $D = 0$, but the v - j curve for $\mu_0 H_{\text{pin}} = 0 \text{ mT}$ and 5 mT is similar to that for $D = 0.2 \text{ mJ/m}^2$. These results suggest that the direction of DW motion depends not only on D , but also on H_{pin} and j .

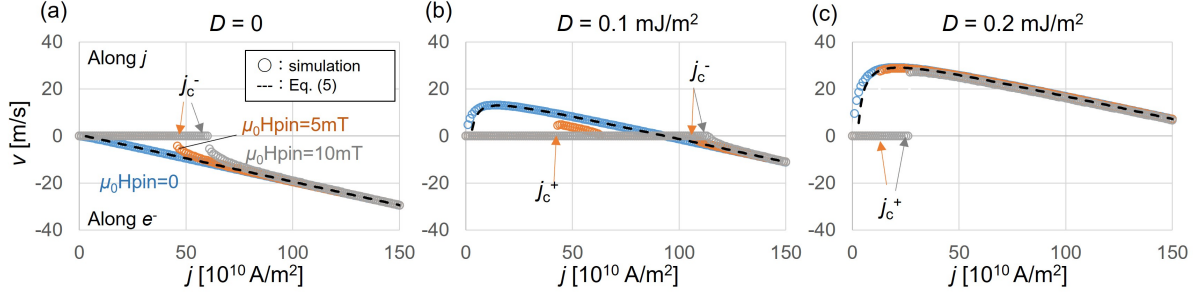


FIG. 5. DW velocity as a function of current density.

The velocity of the quasi-Bloch DW in the absence of extrinsic DW pinning is given by the following equation, as derived in F:

$$v = \gamma\lambda \left(\frac{\pi}{2} H_{\text{DMI}} + \xi_{\text{ST}} j \right) \left(1 + \alpha\beta + \alpha \frac{H_{\text{a}}}{\frac{\pi}{2} \xi_{\text{SL}} j} \right). \quad (5)$$

This equation is consistent with the previous study [7]. The calculated results using Eq. (5) are in good agreement with the numerical simulation results of Eq. (4) with $H_{\text{pin}} = 0$, as shown in Fig. 5. In Eq. (5), the term in the second bracket is approximately 1 due to $\alpha \ll 1$, and determinant of the direction of DW motion is the term in the first bracket. Therefore, in an ideal material system without extrinsic DW pinning, the relationship between STT and DMI determines the direction of DW motion. In our model, $H_{\text{DMI}} \geq 0$ and $\xi_{\text{ST}} j \leq 0$ are satisfied, which causes the DW motion in the direction of electron flow due to STT.

It is worth noting that the DW can move in the direction of electron flow even if $D > 0$, as shown in the case $\mu_0 H_{\text{pin}} = 10 \text{ mT}$ in Fig. 5(b). Karnad *et al.* report the observation of CIDWM in the direction of electron flow in Ta/CoFeB/MgO structures with $\Theta_{\text{SH}} < 0$ and $D > 0$ [44], which is opposite to the predicted direction based on the combination of signs for Θ_{SH} and D . This combination is the same as in our W/CoFeB/MgO structures. Since their measurements of D are not very large ($D \sim 0.03 \text{ mJ/m}^2$), it is possible that the same behavior occurs in their samples as in the case of $\mu_0 H_{\text{pin}} = 10 \text{ mT}$ in Fig. 5(b).

Figure 6 shows the magnetization angle of the DW as a function of current density. When the DW does not move ($v = 0$), in some cases, ϕ deviates from the perfect Bloch state by

more than a few degrees. However, when the DW is in motion ($v \neq 0$), although ϕ oscillates, its median value is close to $\pi/2$. The direction of DW motion is determined by the chirality corresponding to the sign of the median value of $\phi - \pi/2$. When the sign of this value is positive (negative), the right (left)-handed chirality is dominant, and the DW moves in the direction of current (electron) flow. It should be noted that even if the DW moves in the direction of electron flow, the motion is primarily driven by SOT. Unlike in STT-driven motion, there is no precessional magnetization rotation in the DW.

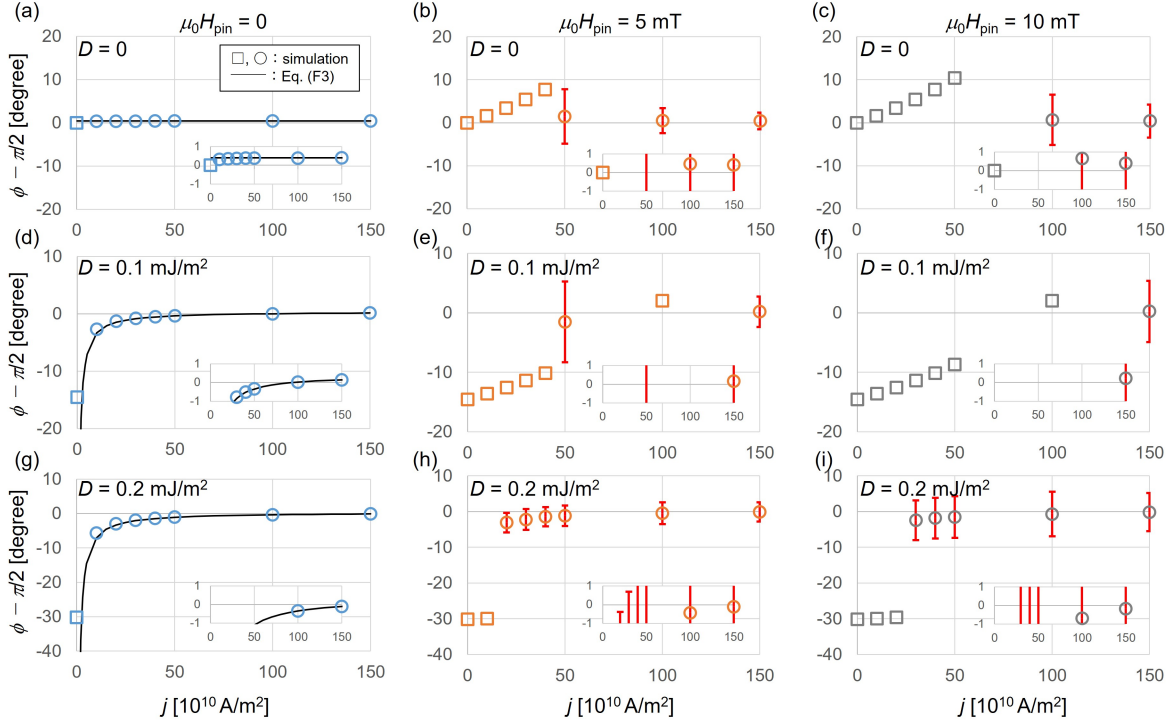


FIG. 6. Magnetization angle of DW as a function of current density. Circle (square) symbols represent the results of $v \neq (=) 0$. The red bars indicate the amplitude of oscillations. The inset provides an enlarged view of the area around $\phi \sim \pi/2$.

Figure 7 shows the threshold current density for DW motion as a function of the extrinsic DW pinning field. Since the behavior of j_c varies depending on the three DMIs ($D = 0, 0.1, 0.2 \text{ mJ/m}^2$), we can classify the regions around these values as weak, intermediate, and strong, respectively. With a weak DMI ($D \sim 0$), the DW motion is in the direction of electron flow, but with a strong DMI ($D \sim 0.2 \text{ mJ/m}^2$), it is in the direction of current flow. In these cases, j_c continuously increases with increasing H_{pin} in the range of $0 \leq j \leq 150 \times 10^{10} \text{ A/m}^2$. However, at an intermediate DMI ($D \sim 0.1 \text{ mJ/m}^2$), j_c increases discontinuously at a certain

point, which corresponds to the condition for switching direction of DW motion. With weak extrinsic DW pinning, the DW can move in the direction of current flow, but with strong extrinsic DW pinning, it can only move in the direction of electron flow.

The threshold current density of SOT-driven quasi-Bloch DW is given as follows, as derived in G:

$$j_c^\pm = \frac{1}{\pi |\xi_{\text{SL}}| |\xi_{\text{ST}}|} \left(\frac{\pi}{2} H_{\text{DMI}} \frac{\pi}{2} |\xi_{\text{SL}}| \mp H_{\text{pin}} \frac{\pi}{2} \xi_{\text{FL}} \mp \sqrt{\left(\frac{\pi}{2} H_{\text{DMI}} \frac{\pi}{2} |\xi_{\text{SL}}| \mp H_{\text{pin}} \frac{\pi}{2} \xi_{\text{FL}} \right)^2 \mp 2\pi |\xi_{\text{SL}}| |\xi_{\text{ST}}| H_{\text{pin}} H_a} \right), \quad (6)$$

where superscript “ j_c ” indicates the direction of DW motion (+ and – correspond to the current and electron flow, respectively). The calculated results using Eq. (6) are in good agreement with the numerical simulation results of Eq. (4) as shown in Fig. 7. The observed discontinuity at $D = 0.1 \text{ mJ/m}^2$ corresponds to the condition where the root term of Eq. (6) is zero. Furthermore, the condition for DW motion in the direction of current flow corresponds to the case where inside of the root of j_c^+ in Eq. (6) is positive. In this case, both j_c^+ and j_c^- exist in one structure, as shown in Fig. 7(b). To the best of our knowledge, there has been no actual observations of a phenomenon where the direction of DW motion switches with current intensity, as shown in this calculation. This may due to the fact that the nucleation of magnetic domains by SOT magnetization reversal inhibits the observation of CIDWM in the high-current density region.

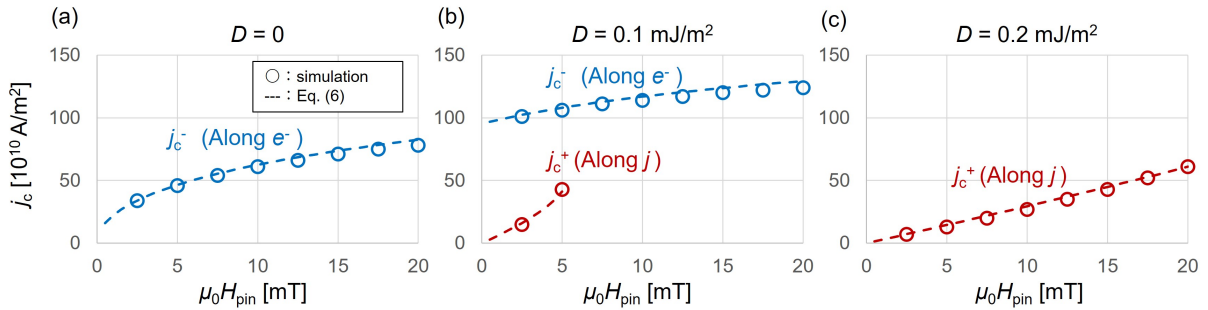


FIG. 7. Threshold current density for DW motion as a function of extrinsic DW pinning field. Superscript “ j_c ” indicates the direction of DW motion (+ and – correspond to the current and electron flow, respectively).

V. SUMMARY

In this study, we investigate the characteristics of SOT-driven motion of quasi-Bloch DWs in perpendicularly magnetized W/CoFeB/MgO ultra-thin films. Our one-dimensional model, incorporating parameters based on the obtained values for the samples, successfully reproduces the experimental results of the direction and threshold current density of DW motion, which exhibit variations among different samples. Our theoretical analysis reveals that during CIDWM, the DW remains in quasi-Bloch-states and the primary driving force is SOT, rather than STT. However, STT significantly influences the direction of DW motion. Additionally, the strength of DMI and extrinsic DW pinning also affect the direction of quasi-Bloch DW motion, in contrast to Neel-type DW motion. These findings provide an explanation for the discrepancy between the experimental direction of DW motion and the expected direction based on the sign combination of DMI and spin Hall angle. Furthermore, our study derives analytical expressions for DW velocity and threshold current density, which can be used to easily predict the characteristics of SOT-driven quasi-Bloch DW motion. These analytical equations will be valuable for designing film structures relevant to DW devices, as they allow for the optimization of low currents and appropriate speeds of DW motion required for future devices.

Appendix A: Vibrating sample magnetometry measurements

We measured the saturation magnetization, M_s and the effective perpendicular magnetic anisotropy, K_{eff} by using vibrating sample magnetometry (VSM). Figure 8 shows the magnetization curves for each sample, and Fig. 9 shows the products of M_s and CoFeB thickness, t_{CFB} as a function of t_{CFB} . By neglecting the annealing temperature dependence of the magnetic dead layer thickness, t_d , we can estimate t_d to be approximately 0.3 nm from Fig. 9. The values of magnetic properties shown in Fig. 1 are evaluated considering the value of t_d .

Appendix B: Depinning field measurements

We determined the depinning field, H_{dep} by conducting magnetic bubble domain expansion experiments following the methodology described in the previous study [24]. In these

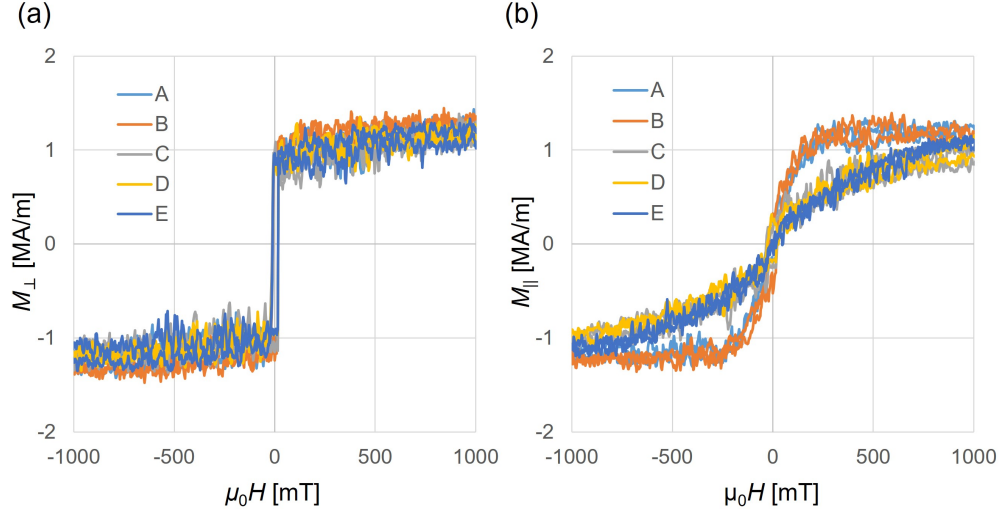


FIG. 8. Magnetization curves measured by VSM. (a) Out-of-plane field, (b) in-plane Field. The labels (A-E) correspond to Table I.

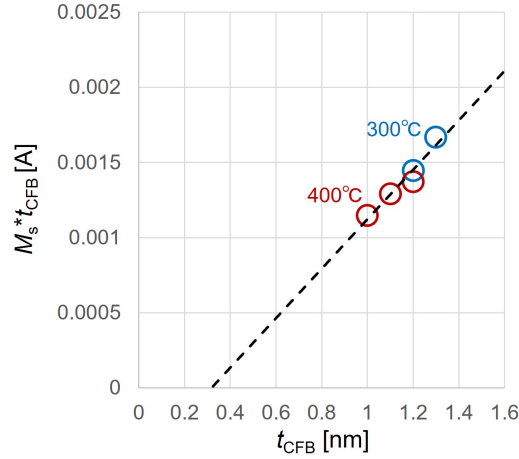


FIG. 9. Products of M_s and CoFeB thickness, t_{CFB} as a function of t_{CFB} .

experiments, we measured the velocity, v of domain wall (DW) in the presence of an out-of-plane applied field, H_z . The domain velocity at temperature, T can be fitted by the following equations in the creep regime ($H_z < H_{\text{dep}}$) and the depinning regime ($H_z > H_{\text{dep}}$) :

$$v(H_z) = \begin{cases} v_{\text{dep}} \exp\left(-\frac{\Delta E}{k_B T}\right) & (H_z < H_{\text{dep}}) \\ \frac{v_{\text{dep}}}{x_0} \left(\frac{T_{\text{dep}}}{T}\right)^\psi \left(\frac{H_z - H_{\text{dep}}}{H_{\text{dep}}}\right)^\beta & (H_z > H_{\text{dep}}) \end{cases} \quad (\text{B1})$$

where $\Delta E = k_B T_{\text{dep}}[(H_z/H_{\text{dep}})^{-\mu} - 1]$ is the creep energy barrier, k_B is the Boltzmann constant, v_{dep} is the DW velocity at $H_z = H_{\text{dep}}$, T_{dep} is the depinning temperature, $\mu = \beta = 1/4$ and $\psi = 0.15$ are the critical exponents, and $x_0 = 0.65$ is the universal constant. Figure 10 shows the DW velocity as a function of H_z for each sample. The value of H_{dep} was obtained by fitting the data using Eq. (B1) with $T = 300$ K assumed.

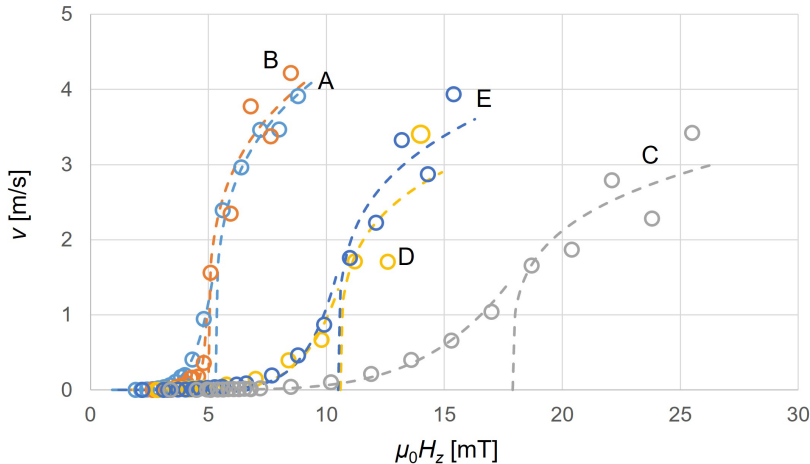


FIG. 10. DW velocity as a function of out-of-plane applied field. The labels (A-E) correspond to Table I. The dotted lines are fitting curves by Eq. (B1).

Appendix C: Dzyaloshinskii-Moriya interaction field measurements

We conducted magnetic bubble domain expansion experiments to measure the Dzyaloshinskii-Moriya interaction (DMI) field H_{DMI} [28, 29]. In these experiments, the velocity of DW, v driven by a pulsed out-of-plane applied field, H_z was measured as a function of the in-plane field, H_x . We measured under the condition $H_z > H_{\text{dep}}$ to ensure that only the influence of H_{DMI} is accounted for in the observation [30]. Figure 11 shows the DW velocity as a function of H_x for each sample. The global minimum of the v - H_x curve is defined as H_{DMI} .

Appendix D: Harmonic Hall voltage measurements

We evaluated the Slonczewski (SL) and field-like (FL) torque efficiencies using harmonic Hall voltage measurements, following the methodology described in the previous study [31]. The frequency, $\omega(2\omega)$ Hall voltage, $V_{\omega(2\omega)}$ was measured under an in-plane field, $H_{x(y)}$ using

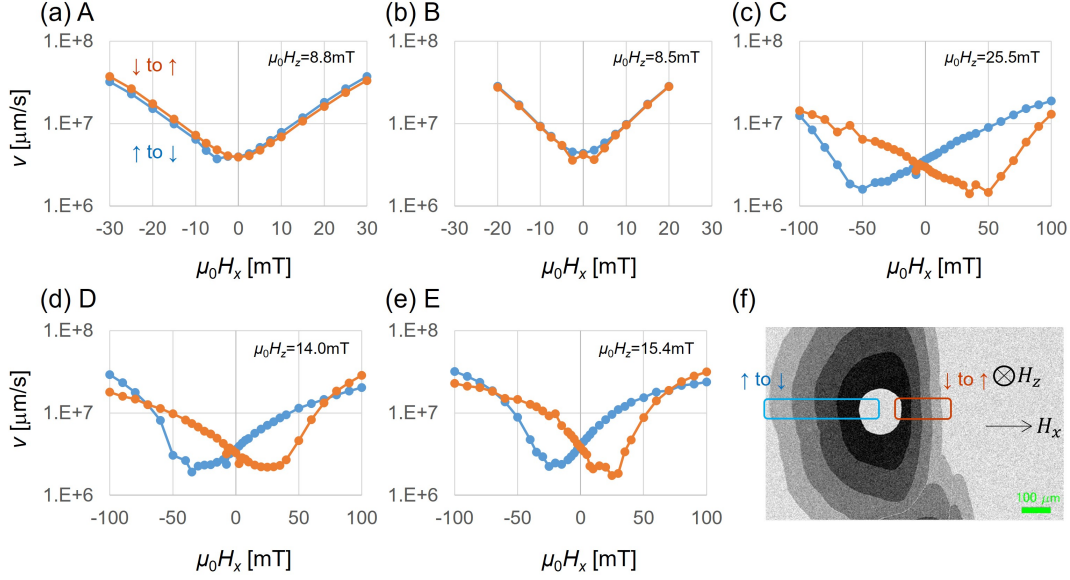


FIG. 11. (a)-(e) DW velocity as a function of the in-plane applied field. The labels (A-E) correspond to Table I. (f) Example of measured magnetic domain with the directions of applied field and magnetic domain indicated.

the experimental setup depicted in Fig. 12(a). The experimental results of the harmonic Hall voltage as a function of $H_{x(y)}$ for each sample are shown in Fig. 12(b). The effective fields for SL and FL torque are denoted as

$$H_{\text{SL(FL)}} = -2 \frac{\partial V_{2\omega} / \partial H_{x(y)}}{\partial^2 V_{\omega} / \partial H_{x(y)}^2} \quad (\text{D1})$$

and SL (FL) torque efficiencies are experimentally defined by $\xi_{\text{SL(FL)}} = \mu_0 H_{\text{SL(FL)}} / j$, where j is the current density. Since the specific resistivity of the CFB and W layers is expected to be roughly similar [7], we assume that the same current density occurs in both layers. When calculating $\xi_{\text{SL(FL)}}$, it is possible to consider a correction for the planar Hall effect (PHE) using the following equation:

$$H_{\text{SL(FL)}}^c = \frac{H_{\text{SL(FL)}} \pm 2\eta H_{\text{SL(FL)}}}{1 - 4\eta^2} \quad (\text{D2})$$

where $\eta = \Delta R_{\text{PHE}} / \Delta R_{\text{AHE}}$ is the ratio of resistivity of PHE to the anomalous Hall effect (AHE). While some researchers suggest that the PHE correction may be unnecessary [33], this study examines cases where the correction is both considered and not considered. If the PHE correction is considered, $\eta = 0.3$ is used as stated in the previous study [34].

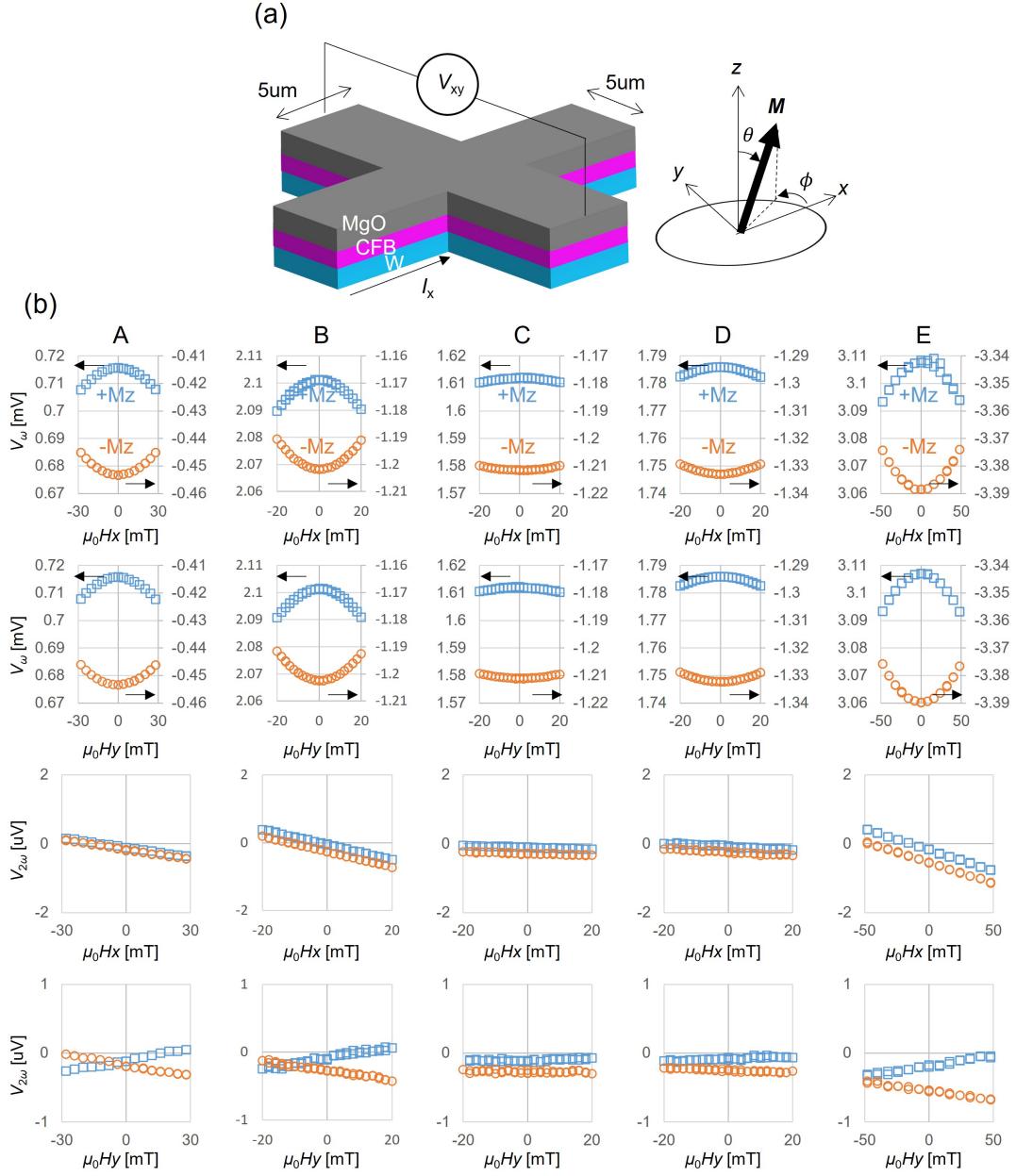


FIG. 12. (a) Schematic illustration of the set up for harmonic Hall voltage measurements and coordinate system. (b) Harmonic Hall voltage versus in-plane field. The labels (A-E) correspond to Table I.

Appendix E: One dimensional model simulation of domain wall velocity

Figure 13 shows the DW velocity, v as a function of current density, j for each sample. The threshold current density of DW motion for each sample is shown in Fig. 3.

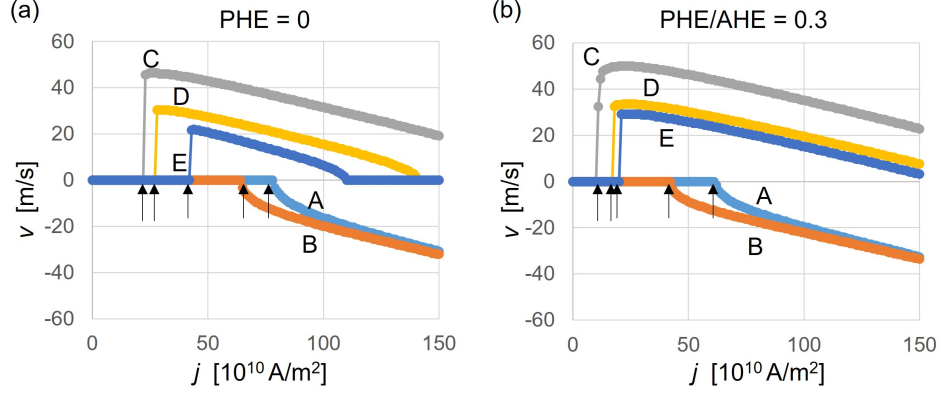


FIG. 13. DW velocity as a function of current density for (a) without and (b) with PHE correction. The labels (A-E) correspond to Table I. Arrows represent the threshold current density, j_c .

Appendix F: Velocity of domain wall motion in the absence of extrinsic pinning

When the DW reaches an equilibrium state in the presence of currents ($d\phi/dt = 0$), the following equation is satisfied based on Eq. (4):

$$a \cos \phi + b \sin \phi - \frac{1}{2}c \sin 2\phi - d = 0, \quad (\text{F1})$$

where $a = \frac{\pi}{2} (\xi_{\text{SL}} - \alpha \xi_{\text{FL}}) j$, $b = Q\alpha \frac{\pi}{2} H_{\text{DMI}}$, $c = \alpha H_{\text{a}}$, and $d = -Q\alpha \xi_{\text{ST}} j$. The stable solution of Eq. (F1) satisfies

$$a \sin \phi - b \cos \phi + c \cos 2\phi < 0. \quad (\text{F2})$$

If the solution to Eq. (F1) is given by $\phi = \pm\pi/2 + \varepsilon$, Eq. (F2) can be approximately written as $\pm\xi_{\text{SL}}j < 0$ when $\alpha \ll 1$, where $\varepsilon(\ll 1)$ is the deviation magnetization angle from Bloch-state. In the following, we consider the case $j > 0$, which leads to $\phi = \pi/2 + \varepsilon$ due to $\Theta_{\text{SH}} < 0$ in our model. By substituting $\phi = \pi/2 + \varepsilon$ into Eq. (F1), we can express

$$\varepsilon \sim \frac{d-b}{c-a} \sim Q\alpha \frac{\frac{\pi}{2} H_{\text{DMI}} + \xi_{\text{ST}} j}{\frac{\pi}{2} \xi_{\text{SL}} j}, \quad (\text{F3})$$

when $\alpha \ll 1$. As shown in Fig. 6, the calculation results using Eq. (F3) are in good agreement with the numerical simulation results of Eq. (4). By substituting Eq. (F3) into Eq. (4), we obtain Eq. (5).

Appendix G: Threshold current density required for domain wall motion

When DW does not move ($d\phi/dt = dX/dt = 0$), the following equations are satisfied based on Eq. (4):

$$a \cos \phi + b \sin \phi - \frac{1}{2}c \sin 2\phi - d + QH_p(X) = 0, \quad (\text{G1})$$

$$e \cos \phi - b \sin \phi + \frac{1}{2}c \sin 2\phi + d + Q\alpha^2 H_p(X) = 0, \quad (\text{G2})$$

where $a = \frac{\pi}{2}(\xi_{\text{SL}} - \alpha\xi_{\text{FL}})j$, $b = Q\alpha\frac{\pi}{2}H_{\text{DMI}}$, $c = \alpha H_a$, $d = -Q\alpha\xi_{\text{ST}}j$, and $e = \alpha\frac{\pi}{2}(\alpha\xi_{\text{SL}} + \xi_{\text{FL}})j$. When $\alpha \ll 1$, we obtain

$$H_p(X) \sim -Q\frac{\pi}{2}\xi_{\text{SL}}j \cos \phi, \quad (\text{G3})$$

and

$$f \cos \phi - b \sin \phi + \frac{1}{2}c \sin 2\phi + d \sim 0, \quad (\text{G4})$$

from Eq. (G1) and (G2), where $f = \alpha\frac{\pi}{2}\xi_{\text{FL}}j$. By substituting $\phi = \pi/2 + \varepsilon$ into Eq. (G4), we can express ε as

$$\varepsilon \sim \frac{d - b}{c + f} = -Q\frac{\frac{\pi}{2}H_{\text{DMI}} + \xi_{\text{ST}}j}{H_a + \frac{\pi}{2}\xi_{\text{FL}}j}. \quad (\text{G5})$$

From Eq. (G3) and (G5), we obtain

$$\frac{\pi}{2}\xi_{\text{SL}}\xi_{\text{ST}}j^2 + \left(\frac{\pi}{2}H_{\text{DMI}}\frac{\pi}{2}\xi_{\text{SL}} + H_p(X)\frac{\pi}{2}\xi_{\text{FL}}\right)j + H_p(X)H_a = 0. \quad (\text{G6})$$

Note that $\xi_{\text{SL}}, \xi_{\text{ST}} < 0$, the solution to Eq. (G5) can be expressed as

$$j = \frac{1}{\pi|\xi_{\text{SL}}||\xi_{\text{ST}}|} \left(\frac{\pi}{2}H_{\text{DMI}}\frac{\pi}{2}|\xi_{\text{SL}}| - H_p(X)\frac{\pi}{2}\xi_{\text{FL}} \pm \sqrt{\left(\frac{\pi}{2}H_{\text{DMI}}\frac{\pi}{2}|\xi_{\text{SL}}| - H_p(X)\frac{\pi}{2}\xi_{\text{FL}}\right)^2 - 2\pi|\xi_{\text{SL}}||\xi_{\text{ST}}|H_p(X)H_a} \right). \quad (\text{G7})$$

For DW motion in the direction of current and electron flow, we substitute $H_p(X) = +H_{\text{pin}}$ and $-H_{\text{pin}}$ into Eq. (G7), respectively. As a result, we finally obtain Eq. (6).

-
- [1] T. A. Moore, I. M. Miron, G. Gaudin, G. Serret, S. Auffret, B. Rodmacq, A. Schuhl, S. Pizzini, J. Vogel, and M. Bonfim, *Appl. Phys. Lett.* **93**, 262504 (2008).
- [2] K.-J. Kim, J.-C. Lee, Yun, G.-H. Gim, K.-S. Lee, S.-B. Choe, and K.-H. Shin, *Appl. Phys. Express* **3**, 083001 (2010).

- [3] I. M. Miron, T. Moore, H. Szabolcs, L. D. Buda-Prejbeanu, S. Auffret, B. Rodmacq, S. Pizzini, M. B. Jan Vogel, A. Schuhl, and G. Gaudin, *Nat. Mater.* **10**, 419 (2011).
- [4] P. P. J. Haazen, E. Murè, J. H. Franken, R. Lavrijsen, H. J. M. Swagten, and B. Koopmans, *Nat. Mater.* **12**, 299 (2013).
- [5] S. Emori, U. Bauer, S.-M. Ahn, E. Martinez, and G. S. D. Beach, *Nat. Mater.* **12**, 611 (2013).
- [6] T. Koyama, H. Hata, K.-J. Kim, T. Moriyama, H. Tanigawa, T. Suzuki, Y. Nakatani, D. Chiba, and T. Ono, *Appl. Phys. Express* **6**, 033001 (2013).
- [7] J. Torrejon, J. Kim, J. Sinha, S. Mitani, M. Hayashi, M. Yamanouchi, and H. Ohno, *Nat. Commun.* **5**, 4655 (2014).
- [8] K.-S. Ryu, S.-H. Yang, L. Thomas, and S. S. P. Parkin, *Nat. Commun.* **5**, 3910 (2014).
- [9] J. Torrejon, E. Martinez, and M. Hayashi, *Nat. Commun.* **7**, 13533 (2016).
- [10] D. Lau and V. Sokalski, *AIP Adv.* **9**, 035208 (2019).
- [11] J. Yoon, S.-H. Yang, J.-C. Jeon, A. Migliorini, I. Kostanovskiy, T. Ma, and S. S. P. Parkin, *Nat. Nanotechnol.* **17**, 1183 (2022).
- [12] K.-S. Ryu, L. Thomas, S.-H. Yang, and S. Parkin, *Nat. Nanotechnol.* **8**, 527 (2013).
- [13] S. Yang, K. Ryu, and S. Parkin, *Nat. Nanotechnol.* **10**, 221 (2015).
- [14] K.-J. Kim, S. K. Kim, Y. Hirata, S.-H. Oh, T. Tono, D.-H. Kim, T. Okuno, W. S. Ham, S. Kim, G. Go, Y. Tserkovnyak, A. Tsukamoto, T. Moriyama, K.-J. Lee, and T. Ono, *Nat. Mater.* **16**, 1187 (2017).
- [15] L. Caretta, M. Mann, F. Büttner, K. Ueda, B. Pfau, C. M. Günther, P. Hession, A. Churikova, C. Klose, M. Schneider, D. Engel, C. Marcus, D. Bono, K. Bagschik, S. Eisebitt, and G. S. D. Beach, *Nat. Nanotechnol.* **13**, 1154 (2018).
- [16] S. Vélez, J. Schaab, M. S. Wörnle, M. Müller, E. Gradauskaite, P. Welter, C. Gutgsell, C. Nistor, C. L. Degen, M. Trassin, M. Fiebig, and P. Gambardell, *Nat. Commun.* **10**, 4750 (2019).
- [17] S. Ranjbar, S. Kambe, S. Sumi, P. V. Thach, Y. Nakatani, K. Tanabe, and H. Awano, *Mater. Adv.* **3**, 7028 (2022).
- [18] Z. Meng, S. He, L. Huang, J. Qiu, T. Zhou, C. Panagopoulos, G. Han, and K.-L. Teo, *Appl. Phys. Lett.* **109**, 142403 (2016).
- [19] P. V. Thach, S. Sumi, K. Tanabe, and H. Awano, *Magnetochemistry* **10** (2024).
- [20] A. Thiaville, S. Rohart, Émilie Jué, V. Cros, and A. Fert, *Europhys. Lett.* **100**, 57002 (2012).

- [21] A. V. Khvalkovskiy, V. Cros, D. Apalkov, V. Nikitin, M. Krounbi, K. A. Zvezdin, A. Anane, J. Grollier, and A. Fert, *Phys. Rev. B* **87**, 020402(R) (2013).
- [22] M. Kim, S.-H. Lee, M. Kim, K. Kim, J. Yoon, J.-H. Park, and S.-B. Choe, *J. Magn. Magn. Mater.* **563**, 169857 (2022).
- [23] V. Jeudy, R. Díaz Pardo, W. Savero Torres, S. Bustingorry, and A. B. Kolton, *Phys. Rev. B* **98**, 054406 (2018).
- [24] J. W. van der Jagt, V. Jeudy, A. Thiaville, M. Sall, N. Vernier, L. Herrera Diez, M. Belmeguenai, Y. Roussigné, S. M. Chérif, M. Fattouhi, L. Lopez-Diaz, A. Lamperti, R. Juge, and D. Ravelosona, *Phys. Rev. Appl.* **18**, 054072 (2022).
- [25] S. Parkin and S.-H. Yang, *Nat. Nanotechnol.* **10**, 195 (2015).
- [26] N. Kato, M. Kawaguchi, Y.-C. Lau, T. Kikuchi, Y. Nakatani, and M. Hayashi, *Phys. Rev. Lett.* **122**, 257205 (2019).
- [27] R. Diaz Pardo, W. Savero Torres, A. B. Kolton, S. Bustingorry, and V. Jeudy, *Phys. Rev. B* **95**, 184434 (2017).
- [28] M. Quinsat, Y. Ootera, T. Shimada, M. Kado, S. Hashimoto, H. Morise, S. Nakamura, and T. Kondo, *AIP Adv.* **7**, 056318 (2017).
- [29] R. Soucaille, M. Belmeguenai, J. Torrejon, J.-V. Kim, T. Devolder, Y. Roussigné, S.-M. Chérif, A. A. Stashkevich, M. Hayashi, and J.-P. Adam, *Phys. Rev. B* **94**, 104431 (2016).
- [30] T. Dohi, S. DuttaGupta, S. Fukami, and H. Ohno, *Appl. Phys. Lett.* **114**, 042405 (2019).
- [31] M. Hayashi, J. Kim, M. Yamanouchi, and H. Ohno, *Phys. Rev. B* **89**, 144425 (2014).
- [32] S. K. Li, X. T. Zhao, W. Liu, T. T. Wang, X. G. Zhao, and Z. D. Zhang, *AIP Advances* **8**, 065007 (2018).
- [33] L. Zhu, D. C. Ralph, and R. A. Buhrman, *Phys. Rev. Lett.* **122**, 077201 (2019).
- [34] W. Skowroński, M. Cecot, J. Kanak, S. Ziętek, T. Stobiecki, L. Yao, S. van Dijken, T. Nozaki, K. Yakushiji, and S. Yuasa, *Applied Physics Letters* **109**, 062407 (2016).
- [35] R. Lo Conte, E. Martinez, A. Hrabec, A. Lamperti, T. Schulz, L. Nasi, L. Lazzarini, R. Mantovan, F. Maccherozzi, S. S. Dhesi, B. Ocker, C. H. Marrows, T. A. Moore, and M. Kläui, *Phys. Rev. B* **91**, 014433 (2015).
- [36] C. Balan, J. W. van der Jagt, J. Peña Garcia, J. Vogel, L. Ranno, M. Bonfim, D. Ravelosona, S. Pizzini, and V. Jeudy, *Appl. Phys. Lett.* **122**, 162401 (2023).

- [37] D. Giuliano, L. Gnoli, V. Ahrens, M. R. Roch, M. Becherer, G. Turvani, M. Vacca, and F. Riente, *ACS Appl. Electron. Mater.* **5**, 985 (2023).
- [38] G. Tatara, H. Kohno, and J. Shibata, *Phys. Rep.* **468**, 213 (2008).
- [39] G. W. Kim, A. S. Samardak, Y. J. Kim, I. H. Cha, A. V. Ognev, A. V. Sadovnikov, S. A. Nikitov, and Y. K. Kim, *Phys. Rev. Appl.* **9**, 064005 (2018).
- [40] R. A. Khan, P. M. Shepley, A. Hrabec, A. W. J. Wells, B. Ocker, C. H. Marrows, and T. A. Moore, *Appl. Phys. Lett.* **109**, 132404 (2016).
- [41] N.-H. Kim, D.-S. Han, J. Jung, K. Park, H. J. M. Swagten, J.-S. Kim, and C.-Y. You, *Appl. Phys. Express* **10**, 103003 (2017).
- [42] J. Cho, N.-H. Kim, J. Jung, D.-S. Han, H. J. M. Swagten, J.-S. Kim, and C.-Y. You, *IEEE Trans. Magn.* **54**, 1 (2018).
- [43] M. Kado, Y. Tokuda, Y. Ootera, N. Umetsu, M. Quinsat, H. Fukumizu, and T. Kondo, *IEEE Trans. Magn.* **59**, 1 (2023).
- [44] G. V. Karnad, F. Freimuth, E. Martinez, R. Lo Conte, G. Gubbiotti, T. Schulz, S. Senz, B. Ocker, Y. Mokrousov, and M. Kläui, *Phys. Rev. Lett.* **121**, 147203 (2018).
- [45] E. Martínez and O. Alejos, *J. Appl. Phys.* **116**, 023909 (2014).
- [46] V. Risinggård and J. Linder, *Phys. Rev. B* **95**, 134423 (2017).
- [47] *J. Magn. Magn. Mater.* **591**, 171674 (2024).
- [48] D. M. Lattery, D. Zhang, J. Zhu, X. Hang, J.-P. Wang, and X. Wang, *Sci. Rep.* **8**, 13395 (2018).
- [49] E. Martinez, *J. Phys.: Condens. Matter* **24**, 024206 (2011).
- [50] The periodic length of extrinsic pinning, L_{pin} does not significantly affect the velocity and the threshold current density of domain wall motion if the order of L_{pin} is same as the width of the domain wall.